

AD-A126 946

ELECTRON SCATTERING FROM SILICON 30(U) AIR FORCE INST  
OF TECH WRIGHT-PATTERSON AFB OH G P BERNHARDT JAN 83  
AFIT/CI/NR-83-3T

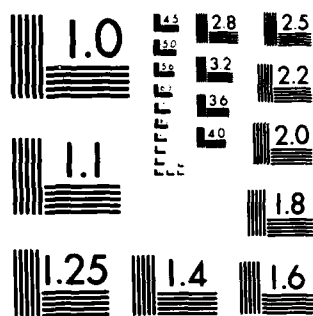
1/1

UNCLASSIFIED

F/G 20/8

NL


END  
DATE  
FILMED  
N. J. P. S.  
DTIC



MICROCOPY RESOLUTION TEST CHART  
NATIONAL BUREAU OF STANDARDS-1963-A

UNCLASS

SECURITY CLASSIFICATION OF THIS PAGE (When Data Entered)

①

REPORT DOCUMENTATION PAGE		READ INSTRUCTIONS BEFORE COMPLETING FORM
1. REPORT NUMBER AFIT/CI/NR 83-3 T	2. GOVT ACCESSION NO. AD-A126946	3. RECIPIENT'S CATALOG NUMBER
4. TITLE (and Subtitle) Electron Scattering from Silicon 30		5. TYPE OF REPORT & PERIOD COVERED THESIS/DISSERTATION
		6. PERFORMING ORG. REPORT NUMBER
7. AUTHOR(s) George Paul Bernhardt IV		8. CONTRACT OR GRANT NUMBER(s)
9. PERFORMING ORGANIZATION NAME AND ADDRESS AFIT STUDENT AT: Massachusetts Institute of Technology		10. PROGRAM ELEMENT, PROJECT, TASK AREA & WORK UNIT NUMBERS
11. CONTROLLING OFFICE NAME AND ADDRESS AFIT/NR WPAFB OH 45433		12. REPORT DATE Jan 83
		13. NUMBER OF PAGES 61
14. MONITORING AGENCY NAME & ADDRESS (if different from Controlling Office)		15. SECURITY CLASS. (of this report) UNCLASS
		15a. DECLASSIFICATION/DOWNGRADING SCHEDULE
16. DISTRIBUTION STATEMENT (of this Report) APPROVED FOR PUBLIC RELEASE; DISTRIBUTION UNLIMITED		
17. DISTRIBUTION STATEMENT (of the abstract entered in Block 20, if different from Report)		
18. SUPPLEMENTARY NOTES APPROVED FOR PUBLIC RELEASE: IAW AFR 190-17 24 Mar 83		
19. KEY WORDS (Continue on reverse side if necessary and identify by block number) LYNN E. WOLAVER Dean for Research and Professional Development AFIT, Wright-Patterson AFB OH		
20. ABSTRACT (Continue on reverse side if necessary and identify by block number) ATTACHED		

DTIC  
SELECTED  
APR 19 1983  
S E

FORM 1 JAN 73 1473

EDITION OF 1 NOV 65 IS OBSOLETE

UNCLASS

83 04 19 005 SECURITY CLASSIFICATION OF THIS PAGE (When Data Entered)

A126946

FILE COPY

DTIC

Mr Copy

83-3

ELECTRON SCATTERING FROM SILICON 30

by

GEORGE PAUL BERNHARDT IV

B.S., UNITED STATES AIR FORCE ACADEMY  
(1979)



SUBMITTED IN PARTIAL FULFILLMENT  
OF THE REQUIREMENTS FOR THE DEGREE  
OF  
MASTER OF SCIENCE

at the

MASSACHUSETTS INSTITUTE OF TECHNOLOGY  
(January, 1983)

Accession For	
NTIS GRA&I	<input checked="" type="checkbox"/>
DTIC TAB	<input type="checkbox"/>
Unannounced	<input type="checkbox"/>
Justification	
By _____	
Distribution/	
Availability Codes	
Dist	Avail and/or Special
A	

Signature of Author..... *George P. Bernhardt IV*.....  
Department of Physics, January 7, 1983

Certified by..... *Claude F. Williams*.....  
Thesis Supervisor

Accepted by.....  
Chairman, Department Committee

## Table of Contents

	Page
I. INTRODUCTION	3
II. ELECTRON SCATTERING THEORY	6
Introduction	6
Kinematics	7
Scattering Form Factor	10
Matrix Formulation	10
Individual Particle Model	15
III. EXPERIMENTAL APPARATUS	19
Introduction	19
Spectrometer and Data Acquisition	20
Targets	22
IV. DATA ANALYSIS	24
Introduction	24
Energy Spectrum	24
Cross Section	29
Form Factor	34
Systematic Errors	36
V. RESULTS AND CONCLUSIONS	40
REFERENCES	59
ACKNOWLEDGEMENTS	61

# ELECTRON SCATTERING FROM SILICON 30

GEORGE PAUL BERNHARDT IV  
1Lt, USAF

1983  
61 pages

S.M. Physics  
MASS. INSTITUTE OF TECHNOLOGY

## ABSTRACT

An electron scattering experiment was performed at the MIT Bates Linear Accelerator facility on a target of naturally occurring silicon. Several of the low-lying inelastic states of  $^{30}\text{Si}$  were examined to determine the single-particle transitions which contribute to the states.

The levels examined were the second, third, eleventh, twelfth, and thirteenth levels. Form factors for each of these states were determined experimentally and the appropriate harmonic oscillator polynomial was then extracted from the form factors. Derived polynomials, using a harmonic oscillator model, for single-particle transitions were then compared to the fitted polynomials.

The second and twelfth levels,  $J^\pi = 2^+$ , were found to be mostly a 2s-1d transition while the third level, also  $J^\pi = 2^+$ , was found to be mostly a 1d-1d transition. The eleventh state,  $J^\pi = 3^-$ , was found to be approximated best by a 1d-1f transition. The thirteenth level,  $J^\pi = 4^+$ , led to the possibility of 1f strength in the  $^{30}\text{Si}$  ground state as other possible transitions are unlikely.

## CHAPTER I

## INTRODUCTION

In 1940, the first experiments on electron excitation of nuclei to discrete levels were done by Collins and Waldman(1.1). The first theoretical discussions of this inelastic electron scattering were due to Mamasachlisor in 1943(1.2) and Snedden and Touschek in 1948(1.3). Lyman et al. in 1951, using a betatron, clearly saw effects due to deviations from point Coulomb scattering, thus allowing nuclear sizes to be measured using electron elastic scattering(1.4). Since that time, linear accelerators have become the standard source of high-energy electrons for such work. However, due to the limited resolution, an experiment of the type done in this thesis was not possible before the current generation of linear accelerators and spectrometers.

The machines used in the 1950's allowed electron scattering with a resolution of  $\Delta p/p$  ( $5 \times 10^{-3}$ ) and with currents of a few tenths of a micro-ampere. Work done using these machines, although including some excellent work such as that done by Hofstadter(1.5) was limited to a few nuclei with well-isolated levels due to inability to resolve closely spaced levels. By the early 1970's, facilities existed with energy resolution of  $\Delta p/p$   $10^{-3}$  with useable currents of 1-2  $\mu$  A. To reach a resolution on the order of  $10^{-4}$  it was necessary to use an energy-loss spectrometer.

In previous systems, high resolution has meant throwing away most of the primary beam on energy defining slits, since the beam incident on the target was analyzed to the level of resolution required for the experiment. Less than one percent of the primary beam was available for resolutions on the order of  $10^{-4}$  since most linear accelerators have an inherent resolution on the order of  $10^{-2}$ . The most important improvement in electron scattering of the last decade has been the recognition that this loss of intensity can be avoided by using energy-loss spectrometry. The two important resolutions in a high precision measurement of an electron scattering cross section are the resolution of the energy-loss of a scattered electron reflecting excitation of nuclear states and the resolution of the momentum transfer to the nucleus. Many experiments, including this one, require the nuclear level resolution  $\Delta E/E$  to be on the order of  $10^{-4}$ , but the definition of momentum transfer is usually adequate at  $\Delta q/q$  on the order of  $3 \times 10^{-3}$ . Energy loss spectrometry exploits this relaxed requirement on momentum transfer resolution, allowing most of the accelerator beam to be used. High resolution is achieved if the accelerator, beam transport and spectrometer form an achromatic system that images the beam on the focal plane. Each monochromatic component is focused on the target. The beam is dispersed spatially at the target to match the spectrometer dispersion(1.6).

Resolutions of the order of  $10^{-4}$  are required to perform  $^{30}\text{Si}$  scattering experiments on a naturally occurring silicon target. Since natural silicon is 92.2%  $^{28}\text{Si}$ , the levels from this isotope will be dominant. Therefore, it is necessary both to resolve  $^{30}\text{Si}$  levels from  $^{28}\text{Si}$  levels and  $^{29}\text{Si}$  levels, and to achieve adequate signal-to-noise to see the  $^{30}\text{Si}$  levels against the background of strong radiative tails from the levels



in  $^{28}\text{Si}$ .

This thesis presents data for electron scattering from several of the low lying states of  $^{30}\text{Si}$ . The form factors for these levels were measured experimentally and compared to a theoretical form factor calculated according to an independent-particle model using harmonic oscillator wave functions. Also, the form factors for the first three states of  $^{28}\text{Si}$  were compared to the results of Whitner(1.7) as a check on the consistency of the data analysis.

Basically, the organization of this thesis is given below. Chapter II presents the theoretical formulation of the form factors using harmonic oscillator wave functions in the reduced matrix. Chapter III presents the experimental apparatus and procedure. Chapter IV covers the data analysis, including extraction of the form factors from the spectra. Chapter V compares the results of Chapters II and IV and gives conclusions.

## CHAPTER II

## ELECTRON SCATTERING THEORY

INTRODUCTION

The importance of electron scattering as a tool for studying nuclear structure cannot be understated. The electron scattering experiments lead directly to an understanding of the electromagnetic structure of nuclei. Three considerations show this importance. First, the electromagnetic interaction between the electron beam and the target is well understood, thus allowing separation of electromagnetic effects and structural effects. This is as opposed to experiments using strongly interacting nuclear projectiles, such as protons, in which neither the interaction nor the structure of the target is well known. Secondly, within the restriction that the four momentum transfer  $[q_\mu = (\vec{q}, \omega)]$  be spacelike, the three momentum transferred to the nucleus ( $\vec{q}$ ) can be varied independently of the nuclear excitation energy, allowing one to map the transition densities to discrete nuclear states in momentum space. Thirdly, in many experiments,

$$\frac{Z e^2}{\hbar c} = Z \alpha = \frac{Z}{137} \quad (1)$$

is small compared to unity, allowing the computation of the transition rate using the Born approximation for exchange of one virtual photon. In such a

case, one can make measurements without greatly disturbing the structure of the target.

This section presents the formalism of electron scattering largely based on the development by Willey(2.1). Emphasis is on the kinematics and the calculation of the form factor using a harmonic oscillator model.

### KINEMATICS

The kinematic parameters are shown in Figure II.1 for an electron-nucleus scattering event. The electron is extremely relativistic at even the lowest incident energy used in this experiment (148 MeV). Hence, the electron rest mass may be ignored since it is only on the order of .5 MeV.

Conservation of linear momentum yields two equations

$$p_i = p_f \cos \theta + q \cos \phi \quad (2)$$

and

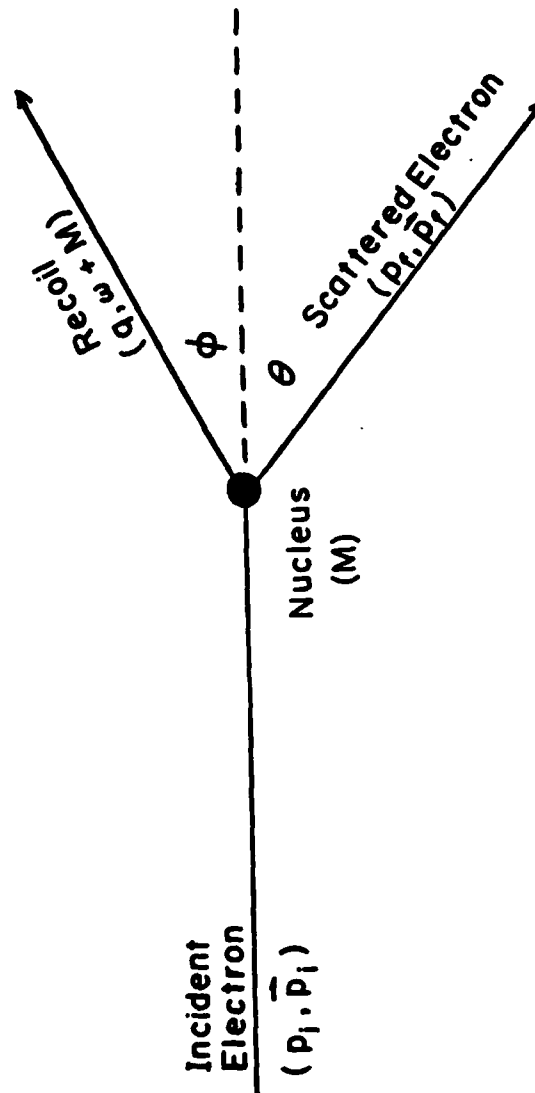
$$0 = p_f \sin \theta + q \sin \phi \quad (3)$$

Conservation of mass and energy, in a relativistic form, yields

$$p_i + M_T = p_f + \sqrt{(M_T + E_x)^2 + q^2} \quad (4)$$

In the above equations  $E_x$  is the excitation energy of the nucleus and  $M_T$  is the rest mass of the nucleus. The other parameters are shown in the figure. Using these equations, one may derive the following expression for

FIGURE II.1  
KINEMATIC PARAMETERS



the final electron momentum:

$$P_f = \frac{P_i - E_x - E_x^2 / 2 M_T}{\left[ 1 + \frac{2 P_i}{M_T} \sin^2 \theta / 2 \right]} \quad (5)$$

The denominator is known as the nuclear recoil factor and is usually denoted by  $\eta$ . If one solved equations 2-4 for  $q$  instead of for  $P_f$ , the results would be

$$q^2 = 4 P_i P_f \sin^2 \frac{\theta}{2} + \omega^2 \quad (6)$$

where

$$\omega = P_i - P_f \quad (7)$$

This leads to the restriction on the four momentum mentioned earlier,

$$q^2 - \omega^2 \geq 0 \quad (8)$$

In analyzing the data, the kinematic shift caused by mass differences between isotopes must be taken into account. The excitation energy scales for the spectra are determined for  $^{28}\text{Si}$ , the dominant isotope. The peaks due to levels in  $^{30}\text{Si}$  will appear on this scale, but will be shifted. The shift arises from the recoil factor  $\eta$  because of the mass difference between  $^{28}\text{Si}$  and  $^{30}\text{Si}$ . The apparent  $^{30}\text{Si}$  levels will appear to be lower than their true energy. If  $E_{x_1}$  is the apparent energy, it is found to be

$$E_{x_1} = \frac{-2 M_1 + \sqrt{4 M_1^2 + 8 M_1 E}}{2} \quad (9)$$

where

$$G = \frac{\rho_i}{\eta_2} \left[ 2 \rho_i \sin^2 \frac{\theta}{2} \left( \frac{1}{M_2} - \frac{1}{M_1} \right) \right] + \frac{\eta_1}{\eta_2} E_{x_2} \left( 1 + \frac{E_{x_2}}{2 M_2} \right) \quad (10)$$

In these equations,  $E_{x_2}$  is the actual excitation energy. The convention is that a subscript 1 relates the factor to  $^{28}\text{Si}$  and a subscript 2 is the actual value.

### SCATTERING FORM FACTOR

#### Matrix Formulation

The interaction between the electron as it scatters and the nucleus leads to nuclear transitions. The invariant interaction matrix element is

$$\langle f | H' | i \rangle = \int A_\mu^e(x) J_\mu^N(x) d^4x \quad (11)$$

Here  $A_\mu^e(x)$ , the electron four-potential, describes the electron current and is composed of a time-like part, the scalar potential  $\phi$  and a space-like part, the vector potential  $\vec{A}$  ( $A_\mu^e(x) = (\phi(x), \vec{A}(x))$ ). The nuclear four-current,  $J_\mu^N(x)$ , is composed of the time-like part, the nuclear transition charge density  $\rho_N(x)$ , and the space-like part composed of two pieces: (1)  $\vec{j}_N(x)$ , the nuclear current transition density, and (2)  $\vec{\nabla} \times \vec{\mu}_N(x)$ , the magnetization transition density ( $J_\mu^N(x) = (\rho_N(x)_{fi}; \vec{j}_N(x)_{fi} + \vec{\nabla} \times \vec{\mu}_N(x)_{fi})$ ).

For a gauge invariant interaction, the nuclear current must be conserved, requiring the constraint

$$\partial J_\mu^N(x) / \partial x^\mu = 0 \quad (12)$$

The Lorentz gauge places the constraint

$$\partial A_\mu^e(x) / \partial x_\mu = 0 \quad (13)$$

and Maxwell's equations require

$$\square A_\mu^e = 4\pi j_\mu^e = e u_f^\dagger \gamma_\mu u_i e^{-iq_\mu x^\mu} \quad (14)$$

where  $\square$  is the d'Alembertian operator,  $j_\mu^e$  is the electron four-current,  $\gamma_\mu$  is the appropriate Dirac matrix,  $q_\mu$  is the four-momentum transfer ( $q_\mu = (\vec{q}, \omega)$ ), and  $u_i$  and  $u_f$  are the initial and final electron spinors. The appropriate Green's function, or propagator, for this equation is, by Bjorken and Drell(2.2),  $-(1/q_\mu^2)$  yielding the solution

$$A_\mu^e(x) = \left( -\frac{4\pi e}{q_\mu^2} \right) e^{-iq_\mu x^\mu} u_f^\dagger \gamma_\mu u_i \quad (15).$$

The transition matrix elements can now be written as

$$\langle f | H' | i \rangle = \left( -\frac{4\pi e}{q_\mu^2} \right) (u_f^\dagger \gamma_\mu u_i) \int e^{-iq_\mu x^\mu} J_\mu^u(x) d^4x \quad (16).$$

The transition probability per unit time is

$$W(t) = \frac{2\pi}{\hbar} \frac{1/2}{2J_i + 1} \sum_{M_f M_i} \sum_{S_f S_i} |\langle f | H' | i \rangle|^2 \rho(E_f) \quad (17)$$

where  $J_i$  is the spin of the initial state,  $M_i$  and  $M_f$  are the initial and final nuclear spin rates,  $S_i$  and  $S_f$  are the initial and final electron spin states, and  $\rho(E_f)$  is the density of final states and is given by

$$K_f^2 d\Omega_f / (2\pi)^3 \hbar c \eta$$

where  $K_f$  is the final electron momentum,  $d\Omega_f$  is the element of solid angle, and  $\eta$  is the recoil factor defined in equation 5. The cross section can

now be written as

$$\frac{d\sigma}{d\Omega} = \frac{1}{2\pi} \left( \frac{K_f}{2\pi\hbar c} \right)^2 \frac{1}{2J_i+1} |\langle f | H' | i \rangle|^2 \quad (18).$$

The cross section may be broken up into components consisting of the coulomb multipole term (c), the transverse electric multipole term (E), and the transverse magnetic multipole term (M) giving

$$d\sigma = \sum_{\lambda=0}^{\infty} d\sigma_{c\lambda} + \sum_{\lambda=1}^{\infty} d\sigma_{E\lambda} + \sum_{\lambda=1}^{\infty} d\sigma_{M\lambda} \quad (19).$$

In this formulation, transverse and longitudinal components are defined relative to the direction of  $\vec{q}$ . In the above equation,  $\lambda$  is the multipolarity of the transition and is given by

$$|J_f - J_i| \leq \lambda \leq J_f + J_i \quad (20).$$

In the present case,  $\lambda = J_f$  since  $J_i = 0$  for  $^{30}\text{Si}$ .

The transverse multipoles arise from a spin flip of the incident beam. Originally, the spins of the electrons are aligned in either the direction of the electrons (+) or opposite the direction (-) or momentum. After scattering, the electrons must conserve momentum and spin. The final state is now a linear combination of initial + and - states. The portion which flipped spin from either plus to minus or minus to plus accounts for the transverse electric and magnetic multipoles. Thus, the longitudinal coulomb multipole results from that portion of the wave function which did not flip spin.

Just as important as the origin of the multipoles is the parity selection rules governing them. The coulomb and transverse electric multipoles have normal parity  $(-1)^\lambda$ , whereas the transverse magnetic multipole has



abnormal parity  $(-1)^{\lambda+1}$ .

Returning to the formalism, the matrix elements from equation 18 become

$$\langle f | M(C\lambda, \mu, q) | i \rangle = \frac{(2\lambda+1)!!}{q^\lambda} \int j_\lambda(qr) Y_{\lambda\mu}(\hat{r}) \rho_N(\vec{r})_{fi} d^3r \quad (21a)$$

$$\begin{aligned} \langle f | M(E\lambda, \mu, q) | i \rangle &= \frac{(2\lambda+1)!!}{q^{\lambda+1}(\lambda+1)} \int [\vec{\nabla} \times \vec{L}_{j\lambda}(qr) Y_{\lambda\mu}(\hat{r}) \\ &\times \left[ \frac{1}{c} \vec{j}_N(\vec{r})_{fi} + \vec{\nabla} \times \vec{\mu}_N(\vec{r})_{fi} \right] d^3r \end{aligned} \quad (21b)$$

and

$$\begin{aligned} \langle f | M(M\lambda, \mu, q) | i \rangle &= -i \frac{(2\lambda+1)!!}{q^\lambda(\lambda+1)} \int [\vec{L}_{j\lambda}(qr) Y_{\lambda\mu}(\hat{r}) \\ &\times \left[ \frac{1}{c} \vec{j}_N(\vec{r})_{fi} + \vec{\nabla} \times \vec{\mu}_N(\vec{r})_{fi} \right] d^3r \end{aligned} \quad (21c)$$

where  $j_\lambda(qr)$  is the spherical Bessel function,  $L$  is  $-i\vec{r} \times \vec{\nabla}$ , and  $Y_{\lambda\mu}$  is the spherical harmonic. These equations reduce by the well-known Wigner-Eckart theorem, which factors out the dependence on the magnetic quantum numbers  $M_i$  and  $M_f$ , to the following:

$$\begin{aligned} \langle J_f M_f | M(\lambda, \mu, q) | J_i M_i \rangle &= (-1)^{J_f - M_f} \begin{pmatrix} J_f & \lambda & J_i \\ -M_f & \mu & M_i \end{pmatrix} \quad (22) \\ &\times \langle J_f || M(\lambda, q) || J_i \rangle \end{aligned}$$

The separated cross sections may now be written as

$$\frac{d\sigma}{d\Omega}(C\lambda) = \frac{1}{2} \left( \frac{d\sigma}{d\Omega} \right)_{\text{MOTT}} \frac{4\pi}{z^2} \frac{q^{2\lambda}}{[(2\lambda+1)!!]^2} B(C\lambda, \vec{q}, J_i \rightarrow J_f) \quad (23a)$$

$$\frac{d\sigma}{d\Omega}(E\lambda) = \frac{1}{\eta} \left( \frac{d\sigma}{d\Omega} \right)_{\text{MOTR}} \left( \frac{1}{2} + \tan^2 \frac{\theta}{2} \right) \frac{4\pi}{z^2} \frac{(\lambda+1) q^{2\lambda}}{\lambda[(2\lambda+1)!!]^2} \quad (23b)$$

$$\times B(E\lambda, \vec{q}, J_0 \rightarrow J_f)$$

and

$$\frac{d\sigma}{d\Omega}(M\lambda) = \frac{1}{\eta} \left( \frac{d\sigma}{d\Omega} \right)_{\text{MOTR}} \left( \frac{1}{2} + \tan^2 \frac{\theta}{2} \right) \frac{4\pi}{z^2} \frac{(\lambda+1) q^{2\lambda}}{\lambda[(2\lambda+1)!!]^2} \quad (23c)$$

$$\times B(M\lambda, \vec{q}, J_0 \rightarrow J_f)$$

where

$$B(\lambda, \vec{q}, J_0 \rightarrow J_f) = \frac{1}{2J_i+1} |\langle J_f || M(\lambda, q) || J_i \rangle|^2 \quad (24)$$

and

$$\left( \frac{d\sigma}{d\Omega} \right)_{\text{MOTR}} = \left[ \frac{2\hbar c z \cos \frac{\theta}{2}}{2 E_i \sin^2 \frac{\theta}{2}} \right]^2 \quad (25)$$

and  $\eta$  is the nuclear recoil term. The factor

$$q^{2\lambda} / [(2\lambda+1)!!]^2 \quad (26)$$

takes out the lowest order of  $q$ -dependence of  $B$ , so that

$$\lim_{\vec{q} \rightarrow \omega} B(M\lambda, \vec{q}, J_0 \rightarrow J_f) = \left( \frac{2J_f+1}{2J_0+1} \right) B_0(M\lambda, J_f \rightarrow J_0) \quad (27)$$

where  $B_0(M\lambda, J_f \rightarrow J_0)$  is the gamma-ray reduced transition strength. In this notation the form factors may be written as

$$F^2(C\lambda, q) = \frac{4\pi}{z^2} \frac{q^{2\lambda}}{[(2\lambda+1)!!]^2} B(C\lambda, \vec{q}, J_0 \rightarrow J_f) \quad (28a)$$

$$F^2(E\lambda, q) = \frac{4\pi}{Z^2} \left( \frac{\lambda+1}{\lambda} \right) \frac{q^{2\lambda}}{[(2\lambda+1)!!]^2} \quad (28b)$$

$$\times \beta(E\lambda, \vec{q}, J_0 \rightarrow J_f)$$

and

$$F^2(M\lambda, q) = \frac{4\pi}{Z^2} \left( \frac{\lambda+1}{\lambda} \right) \frac{q^{2\lambda}}{[(2\lambda+1)!!]^2} \quad (28c).$$

$$\times \beta(M\lambda, \vec{q}, J_0 \rightarrow J_f)$$

#### Individual Particle Model

It is now necessary to develop equation 24 by using an appropriate model. Before applying the model, it is instructive to briefly examine the general case as presented by Donnelly and Walecka(2.3). In second quantization, the multipole operators have the form

$$\hat{M}(\lambda, M, T, T_z, q) = \sum_{\alpha\beta} \langle \alpha | M_{\lambda M T T_z}(q) | \beta \rangle C_{\alpha}^{\dagger} C_{\beta} \quad (29)$$

where  $\alpha$  and  $\beta$  form a complex set of single particle quantum numbers,  $T$  and  $T_z$  refer to isospin and isospin in the  $Z$  direction,  $C_{\alpha}^{\dagger}$  is the creation operator for the state  $\alpha$ , and  $C_{\beta}$  is the destruction operator for the state  $\beta$ . Taking the matrix elements between exact nuclear states yields

$$\langle f | \hat{M}(\lambda, M, T, T_z, q) | i \rangle = \sum_{\alpha\beta} \langle \alpha | M_{\lambda M T T_z}(q) | \beta \rangle \psi_{\alpha\beta}^{fi} \quad (30)$$

where

$$\psi_{\alpha\beta}^{fi} = \langle f | C_{\alpha}^{\dagger} C_{\beta} | i \rangle \quad (31).$$

Equation 30 expresses the matrix element of an arbitrary multipole operator as a linear combination of single-particle matrix elements multiplied by equation 31, which are simple numerical coefficients. The basis of equation 30 can be doubly reduced with respect to both angular momentum and isospin yielding

$$\begin{aligned} \langle f_j J_f^n T_f || M_{\lambda,T}(q) || i_j J_i^n T_i \rangle \\ = \sum_{a,b} \langle a || M_{\lambda,T}(q) || b \rangle \psi_{\lambda,T}^{(fi)}(a,b) \end{aligned} \quad (32).$$

Once the set of numerical coefficients  $\psi_{\lambda,T}^{(fi)}(a,b)$  have been determined, the exact transition matrix element of any multipole operator can be expressed as a linear combination of single-particle matrix elements. In the present case, the transition was assumed to be single-particle only. Therefore,  $\psi_{\lambda,T}^{(fi)}(a,b)$  was assumed to be a delta function.

In the individual particle model, the nucleus is considered to be a collection of nucleons. Therefore, the nuclear charge, current, and magnetization density operators are, in Willey's notation,

$$\rho_N(\vec{r})_{op} = |e| \sum_{j=1}^A \epsilon_j \delta(\vec{r} - \vec{r}_j) \quad (33a)$$

$$\vec{j}_N(\vec{r})_{op} = \frac{|e|\hbar}{2m} \sum_{j=1}^A \left\{ \epsilon_j (\vec{r} - \vec{r}_j) \vec{p}_j \right\}_{sym} \quad (33b)$$

$$\vec{\mu}_N(\vec{r})_{op} = \frac{|e|\hbar}{2m_e} \sum_{j=1}^A \gamma_j \delta(\vec{r} - \vec{r}_j) \vec{\sigma}_j \quad (33c)$$

where

$$\vec{p}_j = -i\hbar \vec{\nabla}_j \quad (34).$$

The symmetrized form for equation 33b is necessary for the nuclear current in order to satisfy hermiticity and the continuity equation

$$\vec{\nabla} \cdot \vec{j}_{fi} = - \frac{\partial \rho_{fi}}{\partial t} = -i\omega_{fi} \rho_{fi} \quad (35).$$

in isobaric spin notation

$$\varepsilon_j = \frac{1}{2} (1 + \tau_{jz}) \varepsilon_p + \frac{1}{2} (1 - \tau_{jz}) \varepsilon_n \quad (36a)$$

$$\gamma_j = \frac{1}{2} (1 + \tau_{jz}) \gamma_p + \frac{1}{2} (1 - \tau_{jz}) \gamma_n \quad (36b)$$

where  $\tau_z = 2\tau_{jz}$ ,  $\varepsilon_p = 1$ ,  $\varepsilon_n = 0$ ,  $\gamma_p = 2.79$  and  $\gamma_n = -1.91$ . Using these results, the multipole operators become

$$M(C\lambda, \mu, q) = |e| \frac{(2\lambda+1)!!}{q^\lambda} \sum_{j=1}^A \varepsilon_j j_\lambda(qr_j) Y_{\lambda\mu}(\hat{r}_j) \quad (37a)$$

$$\begin{aligned} M(E\lambda, \mu, q) = \frac{|e|}{\lambda+1} \frac{(2\lambda+1)!!}{q^\lambda} \sum_{j=1}^A \left\{ \varepsilon_j \left[ -\frac{A}{q} ((\lambda+1) j_\lambda(qr_j) \right. \right. \\ \left. \left. - q r_j j_{\lambda+1}(qr_j) \right) Y_{\lambda\mu}(\hat{r}_j) + \frac{1}{2} \left( \frac{\hbar c q}{m c^2} \right) \left( j_\lambda(qr_j) r_j \frac{d}{dr_j} \right. \right. \\ \left. \left. + \frac{d}{dr_j} r_j j_\lambda(qr_j) \right) Y_{\lambda\mu}(\hat{r}_j) \right] + \gamma_j \frac{1}{2} [\lambda(\lambda+1)]^{1/2} \\ \left. \times \left( \hbar c q / m c^2 \right) j_\lambda(qr_j) Y_{\lambda\lambda\mu}(\hat{r}_j) \cdot \vec{\sigma}_j \right\} \end{aligned} \quad (37b)$$

$$\begin{aligned} M(M\lambda, \mu, q) = \frac{|e|}{\lambda+1} \frac{(2\lambda+1)!!}{q^\lambda} \left( \frac{\hbar c q}{m c^2} \right) \sum_{j=1}^A \left\{ \varepsilon_j \left[ \left( \frac{\lambda+1}{2\lambda+1} \right)^{1/2} j_{\lambda+1}(qr_j) \right. \right. \\ \left. \left. \times Y_{\lambda\lambda+1\mu}(\hat{r}_j) \cdot \vec{\mathcal{L}}_j + \left( \frac{\lambda}{2\lambda+1} \right)^{1/2} j_{\lambda-1}(qr_j) Y_{\lambda\lambda-1\mu}(\hat{r}_j) \cdot \vec{\mathcal{L}}_j \right] \right. \\ \left. + \gamma_j \left[ -\frac{1}{2} \lambda \left( \frac{\lambda+1}{2\lambda+1} \right)^{1/2} j_{\lambda+1}(qr_j) Y_{\lambda\lambda+1\mu}(\hat{r}_j) \cdot \vec{\sigma}_j \right. \right. \\ \left. \left. + \frac{\lambda+1}{2} \left( \frac{\lambda}{2\lambda+1} \right)^{1/2} j_{\lambda-1}(qr_j) Y_{\lambda\lambda-1\mu}(\hat{r}_j) \cdot \vec{\sigma}_j \right] \right\} \end{aligned} \quad (37c)$$

In the above equations,  $j(qr_j)$  is the spherical Bessel function,  $Y_{\lambda\lambda\mu}(\hat{r}_j)$  is the vector spherical harmonics,  $Y_{\lambda\mu}(\hat{r}_j)$  is the spherical harmonics, and  $\vec{\mathcal{L}}_j$  is  $-\mathbf{r}_j \times \vec{p}_j$ .

The last step in developing the form factors is to use a model for the initial and final states of equation 24. In this case, a harmonic oscillator model was used. The reduced matrices have been calculated by

Donnelly and Haxton using this model. The general result is

$$B\left(\frac{e}{m} \lambda, T, q, J_0 \rightarrow J_f\right) = S_m^{(\frac{e}{m})} \gamma^{\lambda+K} e^{-2\gamma} \tilde{p}^2(\gamma) \quad (38),$$

where  $S$  can be related to the gamma ray transition strength,  $\gamma$  is  $\left(\frac{qb}{2}\right)^2$ ,  $b$  is the harmonic oscillator length parameter, and  $\tilde{p}(y)$  is a polynomial of  $y$  whose coefficients are given in the tables by Donnelly and Haxton(2.4).

In this work, the transverse electric and magnetic multipoles are assumed to be very small for the data taken. Hence, only the longitudinal coulomb form factor is calculated in Chapter V.

## CHAPTER III

## EXPERIMENTAL APPARATUS

INTRODUCTION

The data presented in this thesis are the results of an electron-scattering experiment on natural silicon performed at the MIT Bates Linear Accelerator. The discussion in this chapter is limited to a description of those unique features of the facility relevant to this experiment, as the accelerator has been described in detail in the literature (3.1-3.2).

The facility provides an average electron beam current of 2-40  $\mu$ A without sacrificing resolution ( $\sim 2 \times 10^{-4} \frac{\Delta p}{p}$ ) through its unique energy-loss spectrometer. The high beam current was necessary to provide a reasonable measurement of the small experimental cross sections due to the low percentage of  $^{30}\text{Si}$  in the target. In natural silicon, the percentage of  $^{30}\text{Si}$  is only 3.1%. The resolution must also be high enough to provide a reasonable signal-to-noise ratio in the measured spectrum. Without the high beam current and good resolution, the experiment would have been impossible with natural silicon.

### SPECTROMETER AND DATA ACQUISITION

In the Bates energy-loss system, the incident beam dispersal on the target allows the position on the target to be correlated with the incident energy to an accuracy of better than one part in  $10^4$ . A quadrupole singlet controls the dispersion at the target in order to match the dispersion of the beam transport system to that of the spectrometer. In order to achieve  $10^{-4}$  resolution, the scattered electrons are bent through ninety degrees by the split-pole spectrometer in proportion to their momentum and, therefore, their position. This differential bending brings electrons that underwent the same energy loss in the target to a common focus in the spectrometer focal plane(3.3).

In the detector system, an electron passes first through two multi-wire proportional counters, then into two lucite Cerenkov counters. The planar surfaces of all four detectors are at an angle of forty-five degrees to the central ray of the spectrometer.

The first proportional counter has sense wires tapped by three different delay lines read by time-to-digital signal convertors. The drift time of the ions to these wires can be used to measure both the track position and the angle of entry into the chamber. Drift times are measured perpendicular to the plane of the sense wires and, therefore, this counter is known as the vertical drift chamber. The sense wires give information about particle trajectories in the direction of particle momentum.

The second proportional counter is known as the transverse array and has sense wires read on only one delay line in the direction transverse to the momentum of the particle. Since the optics of the spectrometer are point-to-parallel in this plane, this chamber provides a measurement of



the scattering angle of the particle within the acceptance of the spectrometer(3.4).

The coincidence between the two Cerenkov counters provides a start signal for the delay time measurements of the time-to-digital signal converters. A coincidence between two Cerenkov counters is used due to the need for efficiency. The discriminator on each Cerenkov must be set very low for good efficiency, which would result in a high noise background if only one were used. The Cerenkov threshold also discriminates against heavy charged particles whereas a plastic scintillator would not.

Storage of the event parameters (momentum position, vertical angle, and horizontal angle) and event classification are done by the data acquisition programs in the on-line PDP-11 computer. Communication between the PDP-11 and the detectors is done through the Camac Dataway interfaced by a microprogrammed branch driver.

The detection system requires 300 nano seconds to process the information from a given event. Should another event occur during this time span, both the start and the new event are disqualified by the system and stored in a special register. The recorded signals are tested by known timing criteria to determine whether the signals are consistent with a "good" event. Inconsistent signals are also disqualified and stored in registers according to the criterion covering the disqualification.

Typical resolution values for this experiment ranged from  $1.6 \times 10^{-4}$  to  $2.0 \times 10^{-4} \frac{\Delta p}{p}$ , inside the range necessary for  $^{30}\text{Si}$ . Average beam currents on the target during the experiment ranged from 4 to 40  $\mu\text{A}$ , with 20-30  $\mu\text{A}$  most typical.

### TARGETS

The targets used in this experiment were natural silicon crystals provided by Dr. Robert Wolfson and Mr. Paul Grubenskas of Varian Vacuum Division. The targets were etched to their thickness used in the experiment from 10 mil thick blanks using a blend of hydrofluoric, nitric, and acetic acids. No contamination as a result of this process was observed. A carbon elastic peak was observed in three of the data runs used for this analysis. However, this contamination was most likely an impurity in the vacuum system, and not a result of the etching process. The carbon peaks did not interfere with any of the data analysis. No other contamination was observed at the level of this experiment.

An analysis of target thickness was done by Whitner(3.5). Summarizing her work, she found the thickness of the standard target by using the focal plane calibration program, FPCAL 1, described later. The silicon target was used with other targets of known thickness to calculate a fit to the focal plane and accelerator energy parameters of the run. A map of the fit chi-square as a function of target thickness was produced by varying the silicon target thickness in the calibration program. The target thickness corresponding to the minimum of the chi-square was chosen as correct.

Target thicknesses were compared by measuring the form factor of the  $^{28}\text{Si}$  2+ level under the same conditions with the four individual targets. The ratio of these form factors to the standard target form factor was then used to find the other target thicknesses. A summary of the thicknesses according to the measurements of Whitner is shown in Table III.1. Target uniformity was measured by attenuation of 225 MeV electrons from

$^{147}\text{Pm}$  in the material(3.6). The average thickness in the beam spot area was found to vary  $\pm 3\%$  in the center of the target.

Table (3.1)  
Target Thicknesses

Target Thickness (mg/cm <sup>2</sup> )	Uncertainty (%)
26.50	5.0
25.37	5.4
28.83	9.4
31.83	6.4

## CHAPTER IV

### DATA ANALYSIS

#### INTRODUCTION

A raw experimental datum is simply the number of events per detector channel. To relate these events to the form factors of Chapter II, the relationship between the experimental parameters and those scattering properties of interest must be used to reduce the data to useable form. The reduction is done by creating a spectrum of true events as a function of nuclear excitation energy, by finding the area of the peaks in that spectrum, and by then calculating the form factors of those peaks from that area using the known values of target thickness and integrated charge.

#### ENERGY SPECTRUM

In order to determine the nuclear excitation energy corresponding to a given detector channel, it is necessary to use the design parametrization of the spectrometer and the focal plane. In this experiment, two programs were used to achieve the spectrum, FPCAL 1, which determines the focal plane parameters and accelerator energy, and SORT, which combines spectra at the same magnet settings.

FPCAL 1, although used for some time at MIT, has not been documented to the extent given here. The model used in the analysis is Model 1, the model used for the design of the spectrometer. In general, the program performs a least squares fit to determine three focal plane parameters and the bombarding energy.

The kinematics are those of Chapter II with one addition. The relationship between the scattered electron momentum and incident momentum is given by

$$P_f = \frac{P_i - E_x - E_x^2/2M}{1 + \frac{2P_i}{M} \sin^2 \theta/2} - \Delta \quad (39)$$

where  $\Delta$  is the most probable energy loss in the target and all other parameters are the same as in Chapter II. The quantity  $\Delta$  is given by Landau(4.1) as

$$\Delta = \xi [23.16 + \log \xi + 2 \log (P_i / Z_{eff})] \quad (40)$$

where

$$\xi = 1.535 \times 10^{-4} \left( \frac{a}{\cos \theta_c} \right) \frac{\sum_i Z_i}{\sum_i A_i} \quad (41)$$

and

$$Z_{eff} = \sum_i f_i Z_i \quad (42)$$

The quantities in the above equations are defined as  $f_i$  being the fractional abundance of the  $i$ 'th species in the target,  $Z_i$  being the atomic number of the  $i$ 'th species in the target,  $A_i$  being the atomic weight of the  $i$ 'th species in the target,  $\theta_c$  being the angle between the beam and the normal to the target, and  $a$  is the target thickness in  $\text{mg}/\text{cm}^2$ . The

unknown quantity which will be fitted from equation 39 is the incident momentum,  $P_i$ .

The displacement from the central ray along the focal plane is assumed to be

$$X = (x/\delta)_1 \left( \frac{P_f - P_0}{P_0} \right) + (x/\delta\delta)_1 \left( \frac{P_f - P_0}{P_0} \right)^2 \quad (43).$$

Defining  $\epsilon_1$  to be  $(x/\delta\delta)_1 / (x/\delta)_1$ , yields

$$X = (x/\delta)_1 \left( \frac{P_f - P_0}{P_0} \right) \left[ 1 + \epsilon_1 \left( \frac{P_f - P_0}{P_0} \right) \right] \quad (44)$$

where  $x$  is the distance from the central ray,  $(x/\delta)_1$  is the first order dispersion,  $\epsilon_1$  is the second order dispersion,  $P_f$  is defined above, and  $P_0$  is the electron momentum corresponding to the central ray. The form of  $P_0$  is given by

$$P_0 = \Gamma B \quad (45)$$

where  $\Gamma$  is a linear constant with a design value of 66.90 MeV/KG, and  $B$  is the magnetic field strength in KG. The form of  $P_0$  may be revised to include possible non-linearities if necessary. The unknowns from equation 44 which must be fitted are the two dispersion terms. Equation 44 may be solved for  $P_f$  to yield

$$P_f = P_0 \left\{ 1 - \frac{1}{2\epsilon_1} \left[ 1 - \sqrt{1 + \frac{4\epsilon_1 X}{(x/\delta)_1}} \right] \right\} \quad (46).$$

This equation may be expanded and approximated by

$$P_f \approx P_0 \left\{ 1 + \frac{X}{(x/\delta)_1} \left[ 1 - \frac{\epsilon_1 X}{(x/\delta)_1} + 4 \left( \frac{\epsilon_1 X}{(x/\delta)_1} \right)^2 \right] \right\} \quad (47).$$

For the Bates spectrometer,  $\epsilon_1 \approx .4$ ,  $(x/\delta)_1 \approx 372$  inches and  $X \approx 12$  in.

These terms are good initial guesses for the least squares fit. Using

these approximations, equation 47 should be valid to about  $1 \times 15^4$  over the entire focal plane.

The data acquisition code used in this experiment creates, by software, 3072 channels of equal space across the focal plane into which the data are collected. The distance  $X$  can be obtained from the focal plane geometry by the equation

$$X = (1536 - J)W - \left( \frac{Z - F}{1000} \right) \quad (48)$$

where 1536 is the central channel,  $J$  is the channel in question,  $W$  is the width of the channels, presently  $1/128$  in.,  $F$  is the focal plane reference reading, presently 1500, and  $Z$  is the readout value when the focal plane array is positioned so that the central ray passes through the central channel of the focal plane array. In equation 48, the quantity  $Z$  is the quantity which must be fit.

To calibrate the energy spectrum, one must use known peaks in the spectrum to determine the focal plane parameters. Combining equations 44 and 48 and solving for the channel number in which the  $i$ 'th peak falls,  $J_i$  yields

$$J_i = 1536 - \frac{1}{W} \left\{ \left( \frac{Z - F}{1000} \right) + \left( X/\delta_i \right) \left( \frac{P_{fi} - P_o}{P_o} \right) \right. \\ \left. \times \left[ 1 + \epsilon_i \left( \frac{P_{fi} - P_o}{P_o} \right) \right] \right\} \quad (49).$$

The energy of the peak must be known and associated with the  $i$ 'th channel. The program now has a series of known  $J_i$ 's associated with a number of known peaks. A least squares fit is now performed on equation 49, varying the parameters  $P_i$ ,  $Z$ ,  $X/\delta_i$ , and  $\epsilon_i$ . The quantity  $P_i$  is related to the quantity  $P_f$  in equation 49 by equation 39.

The program FPCAL 1 can also take into account the change in momentum from one end of the focal plane to the other. In Model 2, equation 43 becomes

$$X = (x/\delta)_2 \left( \frac{p_f - p_o}{p_f} \right) \left[ 1 + \epsilon_2 \left( \frac{p_f - p_o}{p_o} \right) \right] \quad (50).$$

Solving this equation for  $p_f$  yields

$$p_f = \frac{p_o}{2[(1 - \epsilon_2) - x/(x/\delta)_2]} \left\{ (1 - 2\epsilon_2) + \sqrt{1 - \frac{4\epsilon_2 x}{(x/\delta)_2}} \right\} \quad (51).$$

In equation 51, the first term explicitly takes into account the change in momentum from one end of the focal plane to the other and the second term corrects for spatial variation in this change in width. The procedure from this point on is identical to that of Model 1.

The program SORT uses the focal plane parameters to produce a spectrum of events as a function of excitation energy. The spectra can be reorganized into channels of uniform excitation energy size. Since each detector channel has a spread  $\Delta p/p = 2 \times 10^{-5}$ , the energy size,  $\Delta p$ , depends on the value of  $p$ . A rehistogramming subroutine in the program SORT will reorganize the data into bins of uniform excitation energy width.

The program SORT will also combine data files taken at the same incident energy, scattering angle, and magnet setting, but at different focal plane positions. The distance  $X$  along the focal array is given in terms of a known reference position. Therefore, data from another focal plane position can be added by specifying the new reference position.

The program SORT also uses information about the total charge accumulated in each data run by the beam charge integrators. The integrator



calibration constant is used with this information to determine the events as counts per microcoulomb of incident charge.

The final sorted data file contains the events in counts per microcoulomb as a function of nuclear excitation energy. The energy channels have been reorganized into a constant width across the focal plane. A typical sorted spectrum is shown in Figure IV.1.

### CROSS SECTION

The program FITAB was used to extract the cross sections from the sorted energy spectra. The code uses a least squares fitting routine, by J. Bergstrom, to approximate a line shape to the peak in question. By integrating over some energy range, the peak area can be determined and, thus, the differential cross section may be determined as it is proportional to the peak area.

The shape of the peak can be fit with a deformed Gaussian function of the form

$$P_{\text{peak}} = HT(1 + RX^P) \exp(-2.77 X^2) \quad (52)$$

where HT is the height of the peak, R and P are parameters to be fit, and

$$X = (E - E_{\text{peak}}) / \text{width} \quad (53)$$

where E is the excitation energy (MeV),  $E_{\text{peak}}$  is the excitation energy of the peak, and width is the full width of half maximum. The deformed Gaussian is joined to an inverse polynomial tail of the form

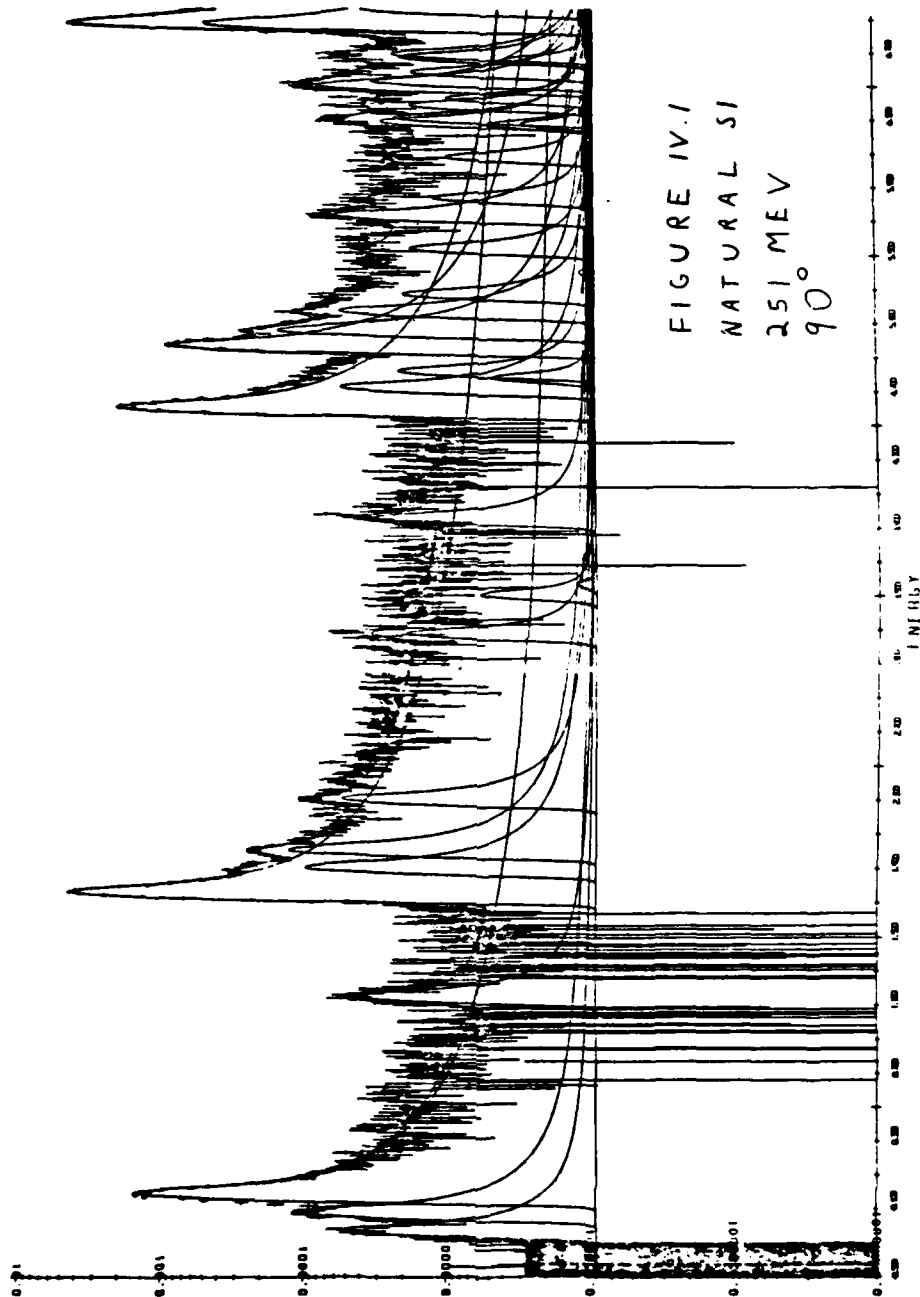


FIGURE IV.1  
 NATURAL SI  
 251 MEV  
 90°

$$Tail = A/x_1 + B/x_1^2 + C/x_1^3 \quad (54)$$

where  $x_1 = X - S$ . These radiative tails, which appear on the lower scattered electron energy side, are mainly due to electrons that have emitted a photon of sufficient energy to reduce their final energy below the energy cutoff. The peaks, in the program, are defined to this cutoff energy, given by  $\Delta E$ , which includes parts of the peak and radiative tail. Radiation tails of preceding peaks form a background to each succeeding inelastic peak in the spectrum. The parameters of the tail function, A and B, are evaluated internally by the program from continuity conditions at the joining point. The radiative tail is joined to the peak function at the point YM, where the total function and its first derivatives must be continuous, and YM is given by

$$YM = (E' - E_{peak}) / width \quad (55)$$

where  $E'$  is the excitation energy at the joining point.

The parameters HT, E peak, width, R, P, S, C, and YM can be varied to minimize the chi-square of the fit. In practice, R, P, S, C, and YM are varied for a reference peak only. These same parameters for all other peaks are then fixed equal to those of the reference peak. This fact ensures that peak shapes do not vary widely from peak to peak. Initial guesses for HT and width were obtained by examination of the sorted spectrum. The initial guess for E peak was the known excitation energy for that peak. The initial guesses for the other five parameters were the default values which have been set by experience.

Background events, including the radiative tails mentioned above, must also be fit to insure proper subtraction. The model used in this experiment is given by

$$Bkgd = A(1) + A(2)z + A(3)z^2 \quad (56)$$

$$z = E - A(4)$$

where the four A parameters can also be varied to minimize the chi-square fit. An inverse polynomial background can also be chosen but was not used in this work.

The errors associated with the fitting technique were also calculated by the program according to the algorithm established by Bevington(4.2) using statistical weighting factors and the inverse derivative matrix.

The peak function and radiative tail are integrated to the cutoff point as mentioned above. At this point, theoretical radiation corrections can be applied to obtain the total peak area(4.3-4.4). These corrections are documented fully by Whitner(4.5) and will be summarized here. The total correction to the experimental cross section can be represented by a multiplicative factor  $C_R$  by

$$\left. \frac{d\sigma}{d\Omega} \right|_{\text{Theory}} = \left. \frac{d\sigma}{d\Omega} \right|_{\text{Exp}} C_R \quad (57)$$

where  $C_R$  is given by  $F_1 F_2 F_3$ .  $F_1$  is the Schwinger factor and is the most important correction. The term arises from the coherent emission and reabsorption of virtual photons by the electron, and the coherent emission of real photons during the scattering event. As stated above, the majority of the radiative tail is from electrons that have emitted a photon of sufficient energy to reduce their final energy below  $\Delta E$ . The term  $F_2$  is

the Bremsstrahlung factor and arises because the electron passes through a target of finite thickness. Hence, the electron can be deflected slightly by other nuclei before and after the scattering event. Thus,  $F_2$  is a "thick target" or incoherent bremsstrahlung correction. Finally,  $F_3$  is the Landau straggling factor. This factor corrects for energy loss straggling which occurs when the electron ionizes an atom in the target. The total peak area, after the corrections have been applied, should be independent of the cutoff energy  $\Delta E$ .

To ensure reasonable values for peak areas, each fit was evaluated on whether the reduced chi-square was small, generally less than 3, and if the corrected peak areas were independent of  $\Delta E$  to better than 3%. This last step was done by using five different cutoff energies. Finally, when very small counting statistic uncertainties meant a large reduced chi-square, the human eye was the final judge of the acceptability of the fit.

After determining the peak area, the differential cross section was calculated by the equation

$$\frac{d\sigma}{d\Omega} = \frac{y_0}{Q} \left( \frac{e}{\Delta\Omega N_t} \right) \quad (58)$$

where  $\frac{y_0}{Q}$  is the peak area in counts/microcoulomb,  $e$  is the charge of one electron,  $\Delta\Omega$  is the spectrometer solid angle acceptance, and  $N_t$  is the number of nuclei in the target per unit area.

The spectrometer solid angle is by horizontal and vertical slits set by the experimenter. Most of the work in this case was done at a horizontal setting of two inches and a vertical setting of ten inches, giving a solid angle of 3.325 milliradians.

The number of target nuclei can be calculated from

$$N_t = \frac{N_0 t_{eff} N}{W} \quad (59)$$

where  $N_0$  is Avogadro's number,  $t_{eff}$  is the effective target thickness in  $\text{mg}/\text{cm}^2$ ,  $N$  is the number of atoms of species per molecule, and  $W$  is the molecular weight of species in  $\text{mg}/\text{moles}$ . The effective target thickness depends on the orientation of the target with respect to the beam. The data were taken at scattering angles of 45 and 90 degrees. This fact allows the targets to be oriented in a transmission mode in the target chamber (Figure IV.2). In this mode, the effective thickness of the target to an electron is independent of where the scattering occurs in the target. An electron scattering anywhere in the target travels through the same amount of material. The effective thickness is given by

$$t_{eff} = t / \cos \theta/2 \quad (60)$$

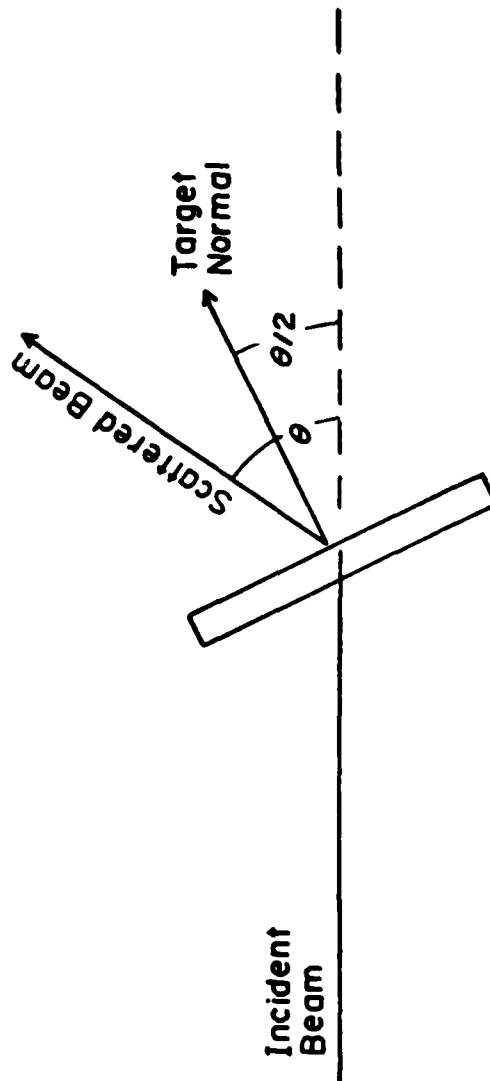
where  $t$  and  $\theta$  are defined in Figure IV.2.

#### FORM FACTOR

The form factor may then be calculated for the differential cross section. The multipole of interest was the coulomb multipole. Since only forward angles were used to take the data, the coulomb term will be much greater than the transverse terms. Combining equations 23a, 24, and 26 from Chapter II yields a differential cross section of the form

$$\frac{d\sigma}{d\Omega} = \frac{1}{\eta^2 z^2} \left( \frac{d\sigma}{d\Omega} \right)_{\text{MOTT}} |F|^2 \quad (61)$$

FIGURE IV.2  
TRANSMISSION MODE



Therefore, the form factor squared may be determined by multiplying the differential cross section by the nuclear recoil factor and by  $Z^2$ , then dividing by the Mott cross section. The program FITAB calculated both the differential cross sections and the form factors.

The polynomial of equation 38 was then extracted by using the program SMFIT. The program uses a least squares fitting routine to determine the coefficients of the polynomial. The parameters of the program are the harmonic oscillator length parameter of Chapter II, the single particle normalizing factor, and the coefficients of the polynomial.

The experimental form factors for a given transition were divided by the terms in front of the polynomial in equation 38. The remaining function was then fitted by a least squares fit to determine the form of the polynomial. The results of the fit could then be compared directly to the tables of Donnelly and Haxton to determine if single particle transitions are realistic approximations to those that occur in  $^{30}\text{Si}$ .

The results of the data analysis are given in Chapter V and discussed in detail there.

#### SYSTEMATIC ERRORS

In addition to the statistical errors from the program FITAB, there are several sources of systematic errors listed in Table 4.1 and discussed below.

Errors from scattering angle measurement, change integration, detector inefficiency, and solid angle measurement are errors resulting from



the limitations in the actual physical measurement of equipment parameters. errors in energy calibration, count-rate corrections, and target parameters are, in principle, difficult to generalize and must be determined separately for each data run. However, in practice the main limitation on experimental accuracy is the precise knowledge of the target thicknesses and uniformities, while other corrections vary little from run to run. Table 4.2 shows the different energies, angles, and targets used to provide the data in this experiment.

The energy calibration uncertainties depend on the individual data run. The error in machine energy measurement was less than .2% for most of the runs.

The uncertainties in the target parameters were determined by Whitner and form the largest contribution to the systematic errors. The target thickness was known to within 5%. The error associated with assuming natural abundances in the target was probably less than 1%.

It is difficult to combine systematic errors from different sources because they do not obey statistical distribution laws. However, the best upper limit estimate of the systematic errors for each data point is 7-10%.

Table 4.1  
Main Sources of Systematic Errors

Machine Energy Calibration	$\pm .3$ MeV
Scattering Angle	$\pm .05$ degrees
Charge Integration	1.0%
Solid Angle	.5%
Overall Detector Inefficiency	2.0%
Dead-time Corrections	.20 (f)
Target Thickness	5-10%
Target Composition	1.0%
Target Uniformity	3.0%

Table 4.2

Incident Energy	Angle (degrees)	Target Thickness (mg/cm <sup>2</sup> )
148.678	45	26.5
174.503	45	26.5
199.141	45	26.5
224.552	45	26.5
166.360	90	26.5
170.814	90	26.5
199.994	90	31.83
228.780	90	26.5
251.036	90	28.83
265.451	90	28.83
279.569	90	26.5
292.968	90	26.5

## CHAPTER V

## RESULTS AND CONCLUSIONS

This chapter will examine each state, comparing the extracted polynomial with the polynomials calculated by Donnelly and Haxton(5.1) using a harmonic oscillator model. Also, the form factors calculated for the first three states of  $^{28}\text{Si}$  will be compared to those of Whitner(5.2) to ensure there are no anomalies in the data.

The form factors extracted from the data by the program FITAB are shown in Tables V.1 through V.6 and in Figures V.1 through V.6. Each figure is divided into two parts. The upper portion is the form factor plotted versus  $q$  effective and the lower portion is the extracted polynomial of Equation 38, which is given as  $\tilde{p}(y)$ . It is this polynomial which may be compared to those derived by Donnelly and Haxton. The form factor plot contains three sets of data, the experimental form factors, the form factors calculated from the fitted polynomial, and the form factors determined in a previous electron scattering experiment by Brain, et al(5.3).

The levels shown are levels two, three, eight, eleven, twelve, and thirteen. The eighth state is an unnatural parity state and is transverse magnetic. Hence, the polynomial,  $\tilde{p}$ , cannot be extracted in the same manner and is not included. Other levels are not included for two reasons. First, for some  $^{30}\text{Si}$  levels, the  $^{28}\text{Si}$  peaks lie too close in the spectrum to allow meaningful separation. Secondly, some  $^{30}\text{Si}$  peaks are so weakly excited that they

FIGURE V.1

LEVEL TWO

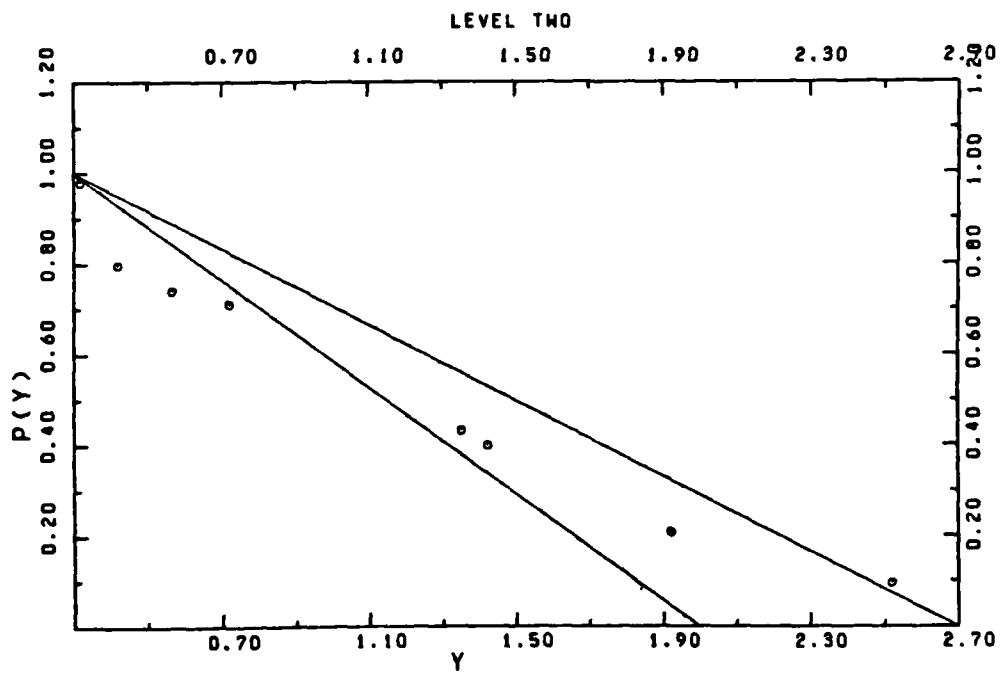
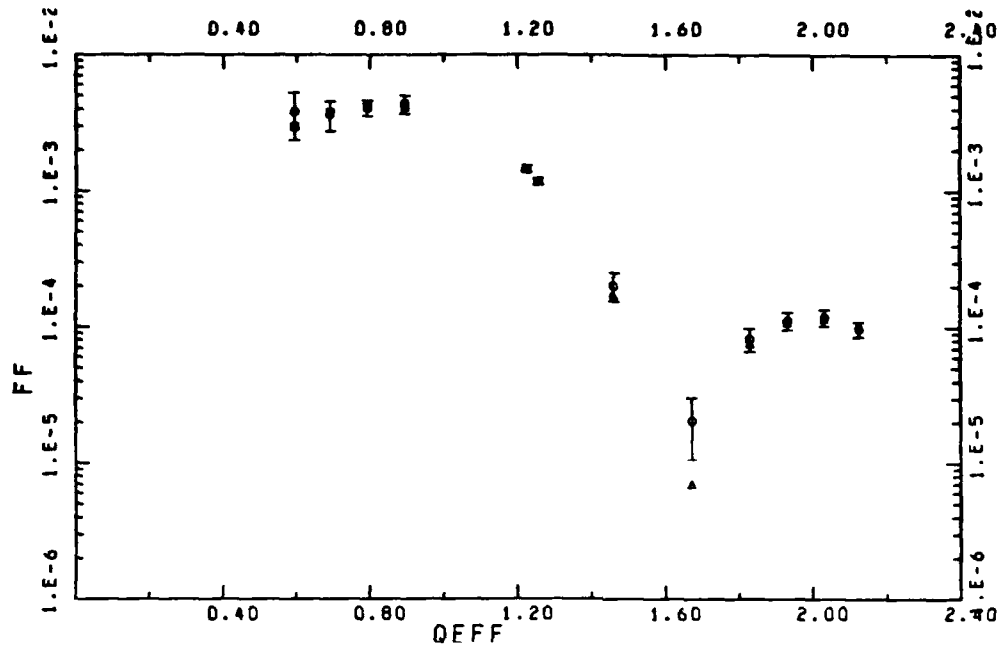


FIGURE V.2  
LEVEL THREE

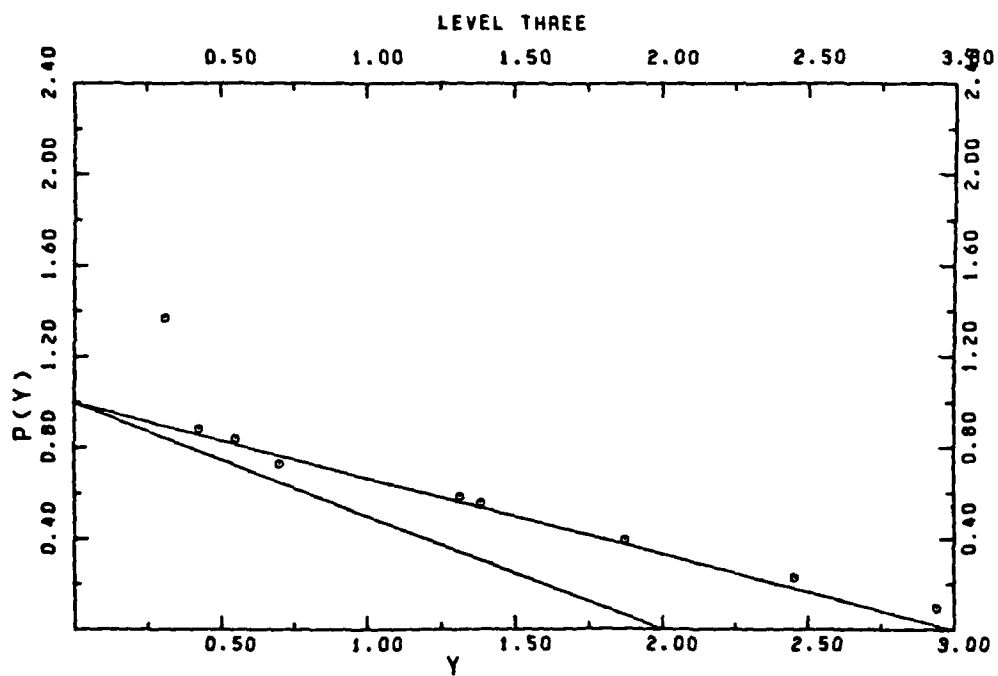
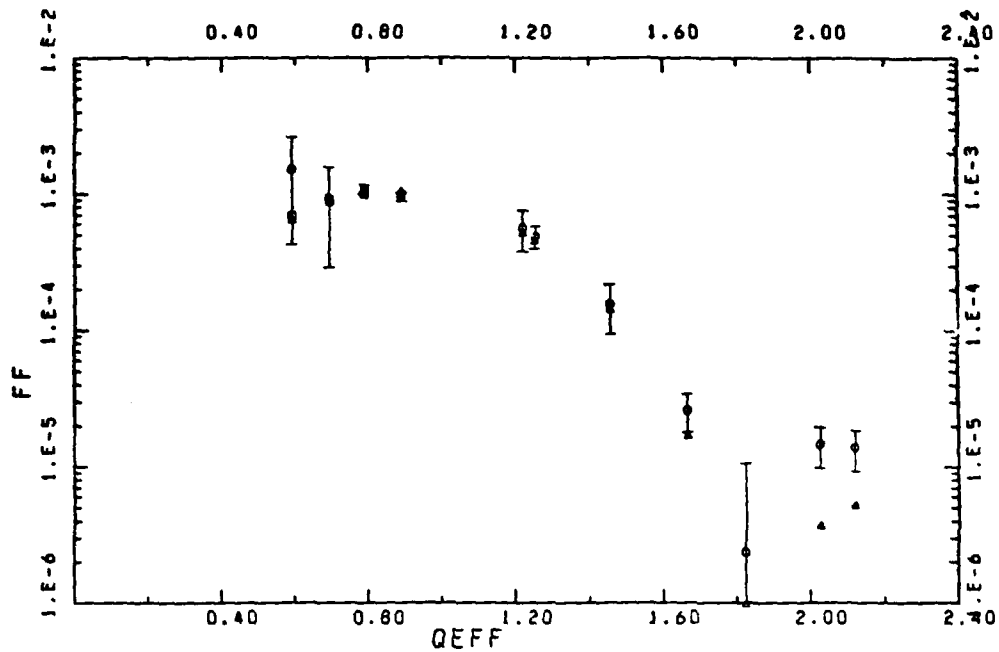


FIGURE V.3

LEVEL EIGHT

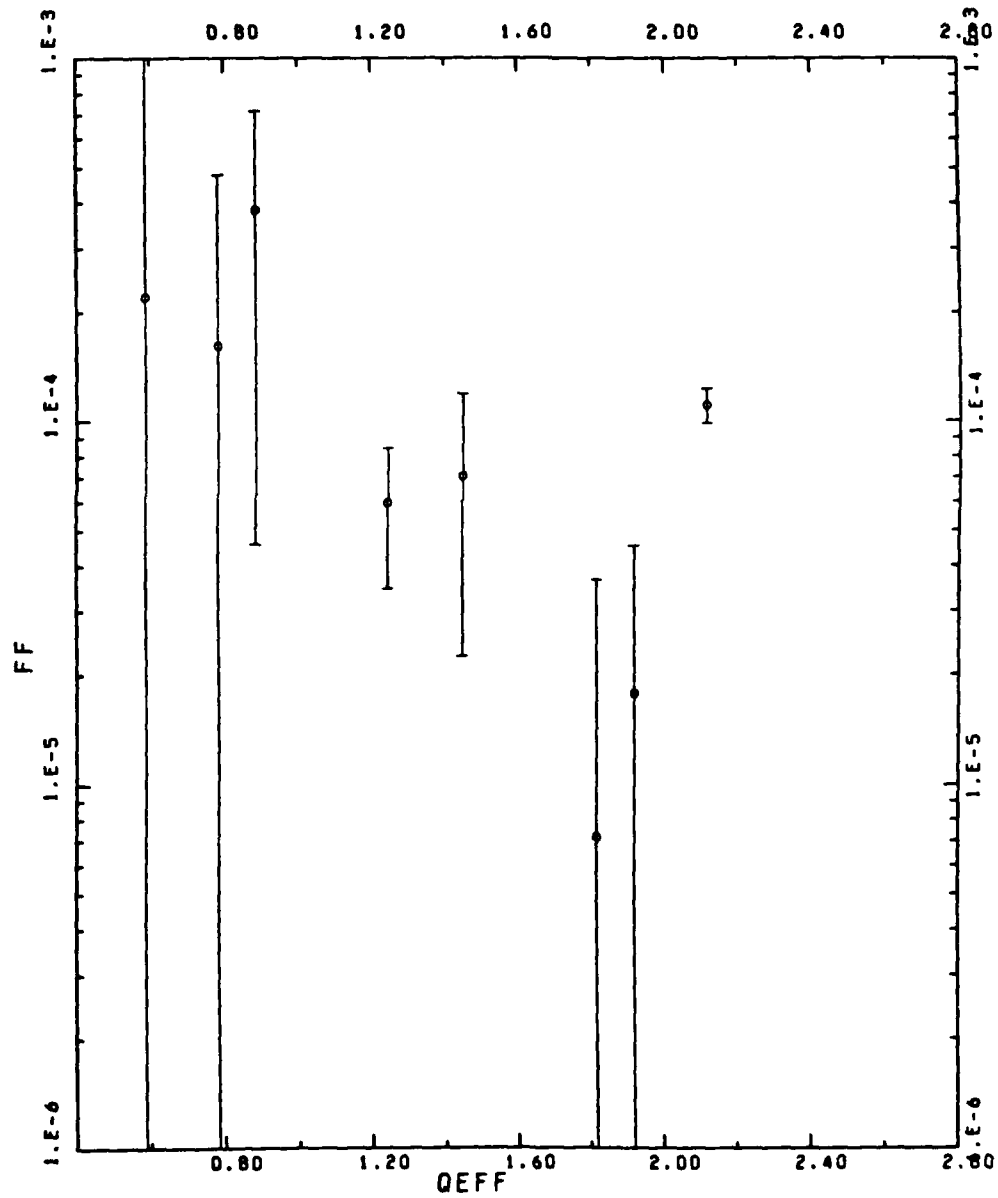


FIGURE V.4  
LEVEL ELEVEN

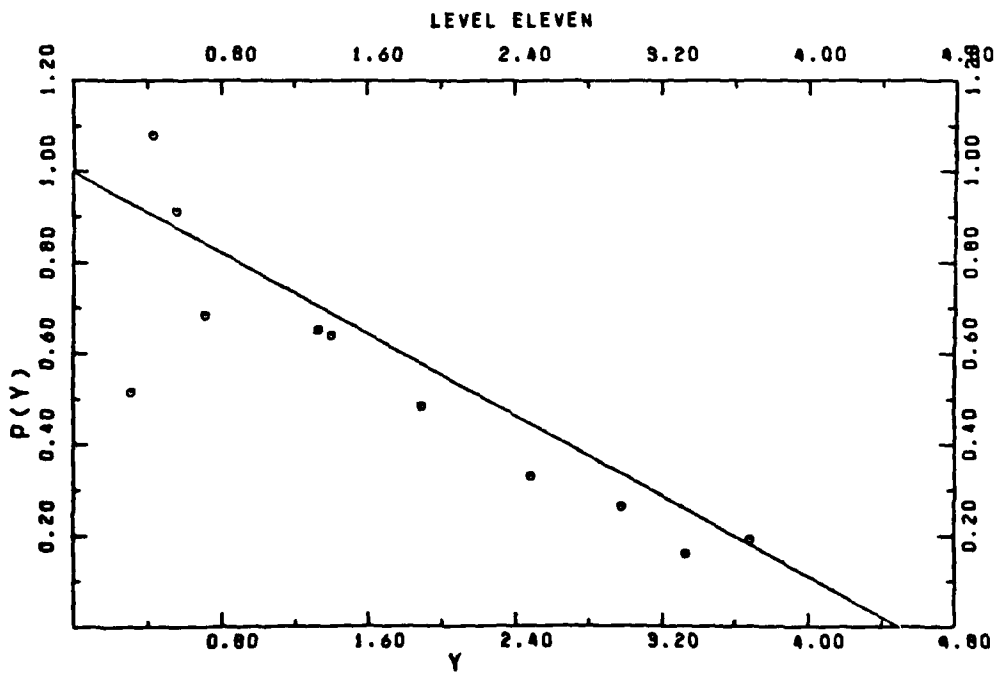
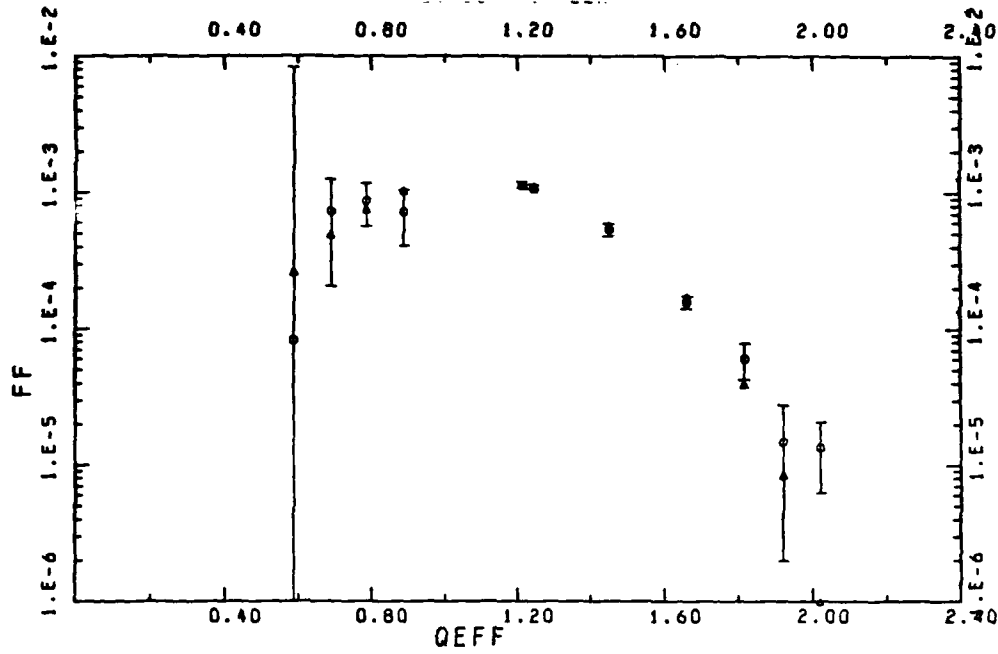




FIGURE V.5  
LEVEL TWELVE

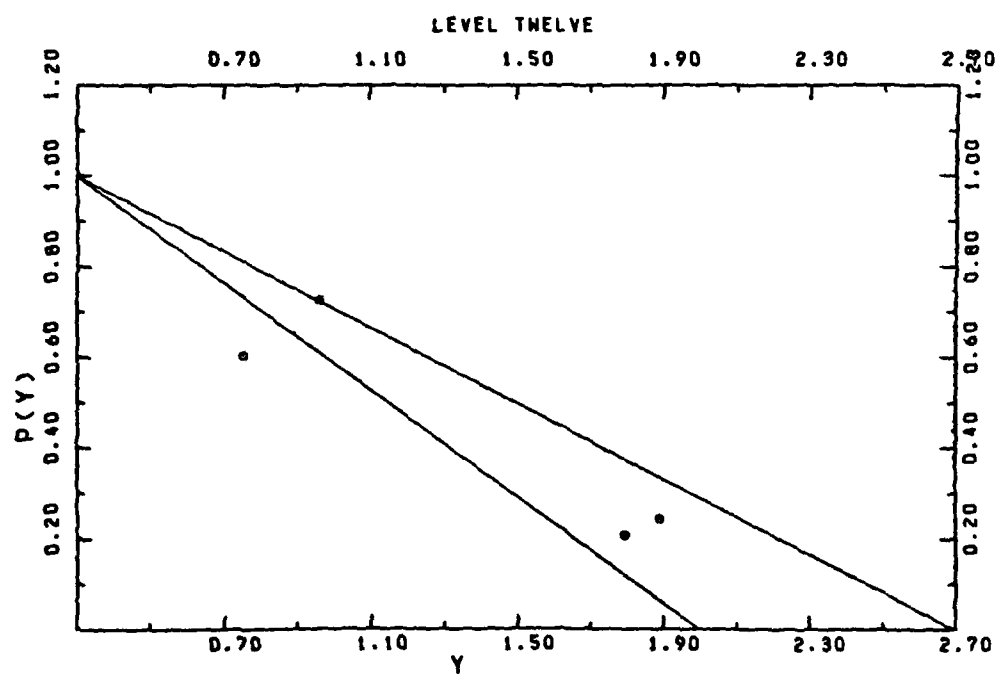
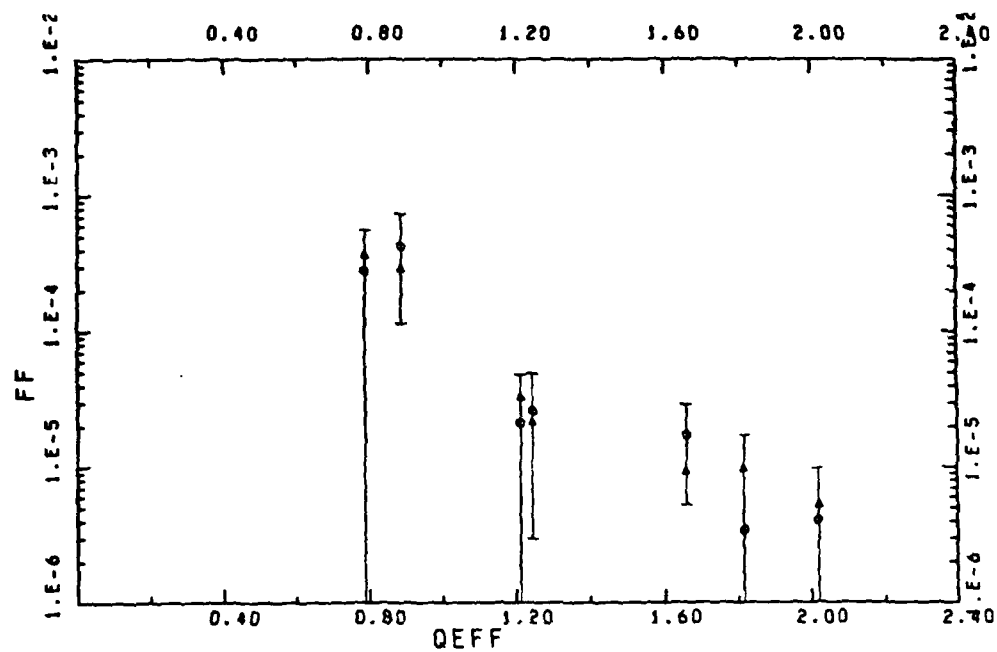


FIGURE V.6  
LEVEL THIRTEEN

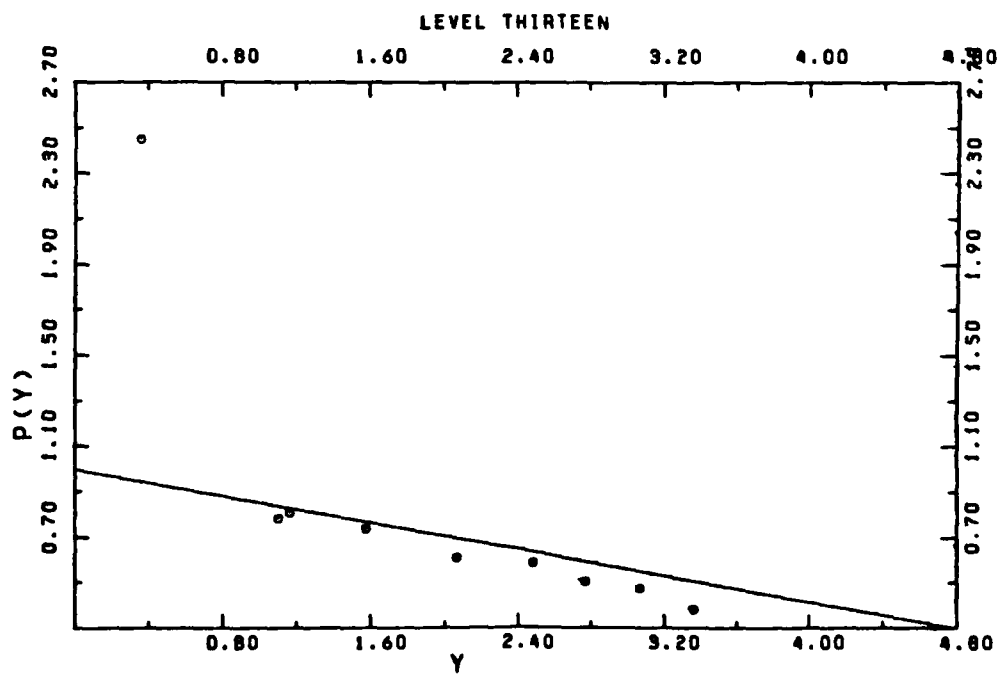
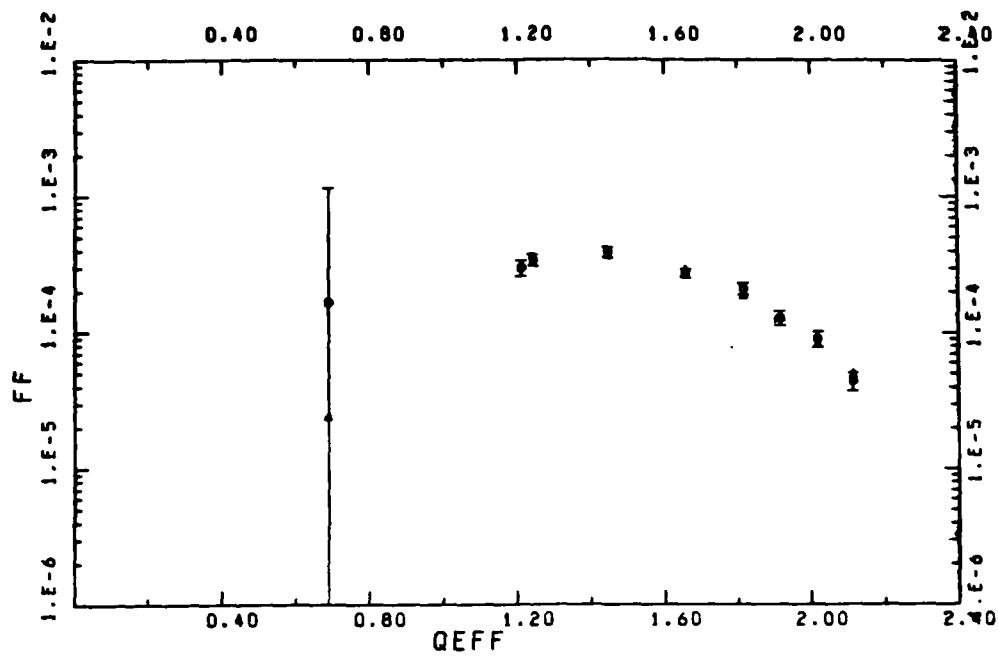


TABLE V.1

Level Two,  $J^\pi = 2^+$ 

Excitation Energy 2.234 MeV

Harmonic Oscillator Length Parameter

 $1.898 \pm .025$  FM

Single Particle Unit Strength

 $9.0081 \pm .1023$ Slope  $-.4197 \pm .0173$ 

Chi Square 1 Deg of Freedom .3817

<u>QEFF</u>	<u>FF</u>	<u>% ERROR</u>	<u>FF CALE</u>	<u>Y</u>	<u>P</u>	<u>+ OR -</u>	
.594	3.83E-3	38.376	3.01E-3	.3177	.979	.173	.21
.691	3.66E-3	24.494	3.86E-3	.4300	.798	.0924	.105
.792	4.07E-3	13.180	4.31E-3	.5648	.741	.0473	.0506
.894	4.35E-3	15.276	4.19E-3	.7197	.711	.0524	.0566
1.226	1.46E-3	5.861	1.45E-3	1.3535	.434	.0125	.0129
1.258	1.18E-3	5.693	1.19E-3	1.4251	.400	.0112	.0116
1.461	2.02E-4	23.788	1.72E-4	1.9221	.209	.0236	.0266
1.072	2.07E-5	48.809	7.04E-6	2.5174	.0967	.0213	.0275
1.829	8.27E-5	19.814	7.67E-5	3.0124	-.274	.026	.0287
1.932	1.13E-4	14.947	1.10E-4	3.3612	-.417	.031	.0324
2.032	1.20E-4	13.470	1.17E-4	3.7181	-.568	.037	.0396
2.126	9.87E-5	12.452	1.06E-4	4.0701	-.684	.0413	.0440

TABLE V.2

Level Three,  $J^\pi = 2^+$ 

Excitation Energy 3.499 MeV

Harmonic Oscillator Length Parameter 1.880 FM

Single Particle Unit Strength  $1.811 \pm .0783$ Slope  $-.3319 \pm .0397$ 

Chi Square 1 Deg of Freedom 1.4224

<u>QEFF</u>	<u>FF</u>	<u>% ERROR</u>	<u>FF CALC</u>	<u>Y</u>	<u>P</u>	<u>+ OR -</u>
.592	1.53E-3	74.835	6.62E-4	.3097	1.37	.440 .680
.694	9.38E-4	69.047	8.90E-4	.4256	.882	.265 .391
.790	1.09E-3	8.210	1.03E-3	.5515	.839	.0338 .0352
.892	9.59E-4	7.401	1.06E-3	.703	.729	.026 .027
1.221	5.75E-4	33.611	5.33E-4	1.317	.585	.091 .108
1.253	4.97E-4	19.011	4.67E-4	1.387	.557	.051 .055
1.456	1.59E-4	40.165	1.47E-4	1.873	.393	.072 .089
1.667	2.64E-5	31.957	1.73E-5	2.4554	.229	.034 .040
1.825	2.36E-6	360.343	1.38E-7	2.943	.096	.110 -
2.027	1.48E-5	33.376	3.77E-6	3.640	-.406	.063 .074
2.122	1.40E-5	34.239	5.28E-6	3.978	-.523	.083 .098

TABLE V.3

Level Eight,  $J^\pi = 3^+$ 

Excitation Energy      5.23 MeV

<u>QEFF</u>	<u>FF</u>	<u>%ERROR</u>
.588	2.20E-4	452.93
.786	1.62E-4	194.17
.889	3.82E-4	87.92
1.247	5.98E-5	41.85
1.45	7.10E-5	68.63
1.818	7.21E-6	411.93
1.921	1.79E-5	155.35
2.115	1.11E-4	11.046

TABLE V.4

Level Eleven,  $J^\pi = 3^-$       Excitation Energy   5.487 MeV  
 Harmonic oscillator Length Parameter   1.901 $\pm$  .146fm  
 Single Particle Unit Strength   7.9467 $\pm$  .511  
 Slope   -.2639 $\pm$  .1088      Chi Square/Deg of Freedom   .937

<u>QEFF</u>	<u>FF</u>	<u>%ERROR</u>	<u>FF CALC</u>	<u>Y</u>	<u>P</u>	<u>+ OR -</u>
.588	8.25E-5	1096.5	2.63E-4	.312	.516	1.27 -
.690	7.36E-4	73.06	4.96E-4	.430	.98	.34 .52
.786	8.72E-4	35.51	7.60E-4	.558	.91	.15 .18
.888	7.28E-4	45.31	1.03E-3	.712	.68	.14 .18
1.214	1.14E-3	5.08	1.13E-3	1.3314	.66	.02 .02
1.246	1.10E-3	4.665	1.07E-3	1.4025	.64	.02 .02
1.449	5.41E-4	9.017	5.73E-4	1.897	.48	.02 .02
1.66	1.59E-4	10.938	1.72E-4	2.489	.33	.01 .02
1.817	6.11E-5	30.661	3.97E-5	2.9805	.26	.04 .04
1.92	1.50E-5	87.96	8.52E-6	3.3302	.16	.06 .10
2.02	1.36E-5	54.029	2.72E-7	3.6861	.19	.04 .06

TABLE V.5

Level Twelve,  $J^\pi = 2^+$       Excitation Energy   5.613 Mev

Harmonic Oscillator Length Parameter   2.21† .178 FM

Single Particle Unit Strength   1.0227† .2438

Slope   -.411      Chi Square/Deg of Freedom   .3187

<u>QEFF</u>	<u>FF</u>	<u>%ERROR</u>	<u>FF CALC</u>	<u>Y</u>	<u>P</u>	<u>+</u> <u>OR</u> <u>-</u>
.786	2.79E-4	102.577	3.66E-4	.7546	.603	.255   -
.888	4.25E-4	73.02	2.95E-4	.9631	.727	.229   .349
1.213	2.14E-5	128.25	3.34E-5	1.797	.209	.107   -
1.245	2.60E-5	88.95	2.19E-5	1.8932	.242	.091   .162
1.659	1.73E-5	71.69	9.46E-6	3.362	.515	.160   .24
1.817	3.47E-6	412.06	9.99E-6	4.032	.387	.489   -
2.019	4.08E-6	144.789	5.39E-6	4.97	.92	.514   -

TABLE V.6

Level Thirteen,  $J^\pi = 4^+$       Excitation Energy   5.95 MeV  
 Harmonic Oscillator Length Parameter   1.737  $\pm$  .126 FM  
 Single Particle Unit Strength      5.9952  $\pm$  .3861  
 Slope   -0.1766  $\pm$  .099      Chi Square/Deg of Freedom   .517

<u>QEFF</u>	<u>FF</u>	<u>% ERROR</u>	<u>FFCALC</u>	<u>Y</u>	<u>P</u>	<u>+</u> OR <u>-</u>
.69	1.67E-4	649.39	2.45E-5	.359	2.45	4.26   -
1.212	2.99E-4	13.862	3.15E-4	1.107	.784	.05   .05
1.244	3.44E-4	10.466	3.32E-4	1.166	.809	.04   .04
1.447	3.90E-4	12.03	3.72E-4	1.578	.739	.04   .04
1.658	2.72E-4	7.076	2.91E-4	2.073	.613	.02   .02
1.816	2.11E-4	10.569	1.91E-4	2.487	.588	.03   .03
1.918	1.29E-4	12.378	1.31E-4	2.77e8	.506	.03   .03
2.018	9.07E-5	13.793	8.35E-5	3.07	.477	.03   .03
2.113	4.45E-5	15.144	4.99E-5	3.3665	.383	.028   .03



are lost in the radiative tails and in the background.

Tables V.7 through V.9 show the experimental form factors for  $^{28}\text{Si}$  extracted in the present analysis and the form factors obtained by Whitner(5.4). The two sets compare very well. Minor differences in the form factors can be accounted for by the fact that Whitner was unable to fit all levels in a single computer run. Hence, at higher  $q$  the radiative tails and background must be approximated. The comparison indicates that no anomalies have crept into the data from any of the programs used.

It is known the  $^{30}\text{Si}$  is not a perfectly spherical nucleus. Therefore, the  $^{30}\text{Si}$  states are most probably admixtures of various spherical shell model components. Comparing the extracted polynomials with those derived by Donnelly and Haxton places experimental limitations on the possible admixtures of spherical shell model states.

In general, one cannot identify uniquely a transition from the shape of its fitted polynomial. In particular, any first-order polynomial can be generated as a linear combination of two or more arbitrary first-order polynomials. However, if the fitted polynomial lies close to one of the derived polynomials corresponding to a particular single-particle transition, there is a strong suspicion that this particular single-particle configuration contributes significantly to the transition. An accidental fit due to particular combinations of other single-particle transitions cannot be ruled out, but such combinations are rather unlikely. It is in this spirit that the identifications discussed below are made.

The excited state in  $^{30}\text{Si}$  is  $J^\pi = 2^+$ . The fitted polynomial has a slope of  $-.42 \pm .02$  which compares to a slope of  $-.5$  for 2S-1d. The lower portion of Figure V.1 shows the fitted polynomial as well as 2S-1d and 1d-1d transi-

TABLE V.7  
SILICON 28,0.0 MeV

<u>QEFF</u>	<u>FF EXP</u>	<u>WHITNER FF</u>
.6079	1.7741E-3	-
.7015	2.0569E-1	1.995E-1
.7971	1.179E-1	1.147E-1
.8962	6.0985E-2	6.127E-2
1.2346	1.0492E-3	1.058E-3
1.2668	5.6132E-4	5.885E-4
1.4698	6.5732E-4	-
1.6804	8.1412E-4	8.222E-4
1.8380	5.024E-4	4.598E-4
1.8945	2.7193E-4	-
2.0402	1.0750E-4	1.119E-4
2.1437	3.7682E-5	4.173E-5

TABLE V.8  
SILICON 28,1.78 MeV

<u>QEFF</u>	<u>FF EXP</u>	<u>WHITNER FF</u>
.604	2.260E-3	-
.698	5.903E-3	6.166E-3
.794	6.716E-3	6.582E-3
.896	6.910E-3	6.910E-3
1.228	3.232E-3	3.238E-3
1.260	2.714E-3	2.706E-3
1.463	7.217E-4	6.328E-4
1.674	3.424E-5	3.624E-5
1.831	3.484E-5	3.350E-5
1.934	7.947E-5	7.806E-5
2.034	1.044E-4	1.049E-4
2.128	1.077E-4	1.090E-4

TABLE V.9  
SILICON 28,4.62 MeV

<u>QEFF</u>	<u>FF EXP</u>	<u>WHITNER FF</u>
-	-	-
.692	4.33E-5	4.100E-5
.788	6.716E-5	7.312E-5
.890	1.613E-4	1.525E-4
1.217	4.164E-4	4.256E-4
1.250	4.169E-4	4.468E-4
1.453	4.958E-4	4.956E-4
1.663	3.590E-4	3.593E-4
1.821	2.47E-4	2.340E-4
1.923	1.650E-4	1.528E-4
2.023	8.679E-5	8.807E-5
<u>2.118</u>	<u>4.665E-5</u>	<u>4.984E-5</u>

tion polynomials. Also included are representative polynomials for higher transitions,  $2h\omega$ . It is important to note that the form factors, at least in the momentum range considered, can be fitted by a linear polynomial. Hence, the higher order polynomials of the  $2h\omega$  transitions do not contribute. This particular state can be part 1d-1d transition, but the main portion is most likely a 2S-1d transition.

The transition to the second excited state ( $J^{\pi} = 2^{+}$ ) appears to be due more to 1d-1d transitions. The fitted polynomial has a slope of  $-.332 \pm .040$  as compared to a slope of  $-.286$  for 1d-1d transitions. Figure V.2 shows the fitted polynomial as well as the derived polynomials for 2S-1d and 1d-1d transitions.

The eleventh state has  $J^{\pi} = 3^{-}$ . The state appears to be a 1d-1f transition. The fitted polynomial is a straight line with a slope of  $-.264 \pm .109$  as compared to the calculated polynomial slope of  $-.222$ . Other transitions which might contribute are 2S-1f, 2S-2p, and 1d-2p transitions, but the 1d-1f transition appears to be dominant (see Figure V.4). Another possibility for creating a  $3^{-}$  state is a 1p-1d transition. Such a possibility is highly unlikely due to the necessity for a hole buried in a shell below the active shell. Furthermore, this transition cannot account for the entire strength because its polynomial has zero slope, and as indicated above, the fitted polynomial has a finite negative slope.

The twelfth state is  $J^{\pi} = 2^{+}$  and appears to be dominantly a 2S-1d transition, as in the first excited state. The fitted slope is  $-.411 \pm .104$  whereas the slope calculated for a 2S-1d transition is  $-.5$  (see Figure V.5).

The last state is the thirteenth state which has  $J^{\pi} = 4^{+}$ . If the

transition were purely a ld-ld transition, the polynomial would be a horizontal line. However, the polynomial has a slope of  $-.177 \pm .099$ . Since the ld-ld transition does not contribute to this slope, only higher transitions can be responsible. The ld-lg transition, as well as the lf-lf transition, has a slope of  $-.182$  and either or both could possibly be responsible (see Figure V.6). What is needed are data taken at a higher momentum transfer to determine where the minimum occurs.

Several conclusions can be reached by looking at the  $2^+$  states, the  $3^-$  state, and the  $4^+$  state separately. The  $2^+$  states have form factors which are fitted well by linear polynomials. Therefore, the single-particle transitions responsible for these states are transitions within one shell. Transitions of  $2\hbar\omega$  were not detected within this momentum range. The  $3^-$  state appears to be a result of a ld-lf transition. Again, the extracted polynomial is linear. The  $4^+$  state is interesting. It appears as if one of two situations is occurring. Either there is some lf strength in the  $^{30}\text{Si}$  ground state or a single-particle transition of  $2\hbar\omega$  is being seen, a ld-lg transition. Should the ground state have some lf strength, then a lf-lf transition would yield a polynomial with slope  $-.182$ , just as a ld-lg transition would. Due to the large gap between the ld state and the lg state, it is more likely that the ground state has some lf strength.

## REFERENCES

## Chapter I

- 1.1 Collins, G. B., and Waldman, B., Phys. Rev., 57, 1088 (1940).
- 1.2 Mamasachlisov, J. Phys., Moscow, 7, 239 (1943).
- 1.3 Sneddon, I., and Tonschek, B., Proc. Roy. Soc. A, 193, 344 (1948).
- 1.4 Lyman, E., Hanson, A., and Scott, M., Phys. Rev., 84, 626 (1951).
- 1.5 Hofstadter, R., Rev. Mod. Phys., 28, 214 (1956).
- 1.6 Bertozzi, et al., Nuc. Instr. and Meth., 162, 211 (1979).
- 1.7 Whitner, K., S. M. thesis, MIT, (unpub. 1979).

## Chapter II

- 2.1 Willey, R., Nuc. Phys., 40, 529 (1963).
- 2.2 Bjorken, J., and Drell, S., "Relativistic Quantum Mechanics", McGraw-Hill, NY, (1964).
- 2.3 Donnelly, T., and Walecka, J., Ann. Rev. Nuc. Sci. 25, 329 (1975).
- 2.4 Donnelly, T., and Haxton, W., Atomic Data and Nuc. Data Tables 23, 103 (1979).

## Chapter III

- 3.1 W. Bertozzi, et al., IEEE Trans. on Nuc. Sci., NS-14, 191 (1967).
- 3.2 Creswell, C., Ph.D. thesis, MIT, (unpub. 1977).
- 3.3 Bertozzi, (1979), Ibid.
- 3.4 Bertozzi, et al., Nuc. Instr. and Meth., 141, 457 (1977).
- 3.5 Whitner, Ibid.
- 3.6 Liljestrang, R., et al., Nuc. Inst. Meth., 138, 471 (1976).

## Chapter IV

- 4.1 Landan, L., Sov J. Phys. 8, 201 (1944).

- 4.2 Bevington, P., "Data Reduction and Error Analysis for The Physical Sciences", McGraw-Hill, NY, (1969).
- 4.3 Maximon, and Isabelle, Phys. Rev. B136,674 (1964).
- 4.4 Mo, and Tsai, Revs. Mod. Phys. 41,205 (1965).
- 4.5 Whitner, Ibid.

#### Chapter V

- 5.1 Donnelly and Haxton, Ibid.
- 5.2 Whitner, Ibid.
- 5.3 Brain, S., et al., J. Phys. G3,821 (1977).
- 5.4 Whitner, Ibid.



## ACKNOWLEDGEMENTS

I would like to thank my advisor, Dr. Claude Williamson, for his help with this work. Without his help and guidance, I would never have accomplished the work necessary for this thesis. I would also like to thank the staff and members of the Linac group for their help, Kay Whitner whose thesis was of inestimable help, and Shirley Meymaris who waded through my writing and typed this thesis. Lastly, I would like to thank Patricia Bernhardt, my wife, and the rest of my family for their infinite patience with me for the last two years.